ORIGINAL PAPER

Surface-modified iron oxide nanoparticles for adsorption, photodegradation, and selective removal applications

Hussein S. Obaid[1] · Ahmed F. Halbus[1]

Abstract

We explored the factors and mechanisms of the adsorption and photocatalytic activity of iron oxide nanoparticles (Fe_2O_3NPs) coated with poly(sodium 4-styrenesulfonate) sodium salt (PSS), and poly(allylamine hydrochloride) (PAH) polyelectrolytes using the layer-by-layer technique. We synthesized Fe_2O_3NPs using the precipitation method at two calcination temperatures, 200 °C and 500 °C. We studied the activity of bare and surface modified Fe_2O_3NPs toward fluorescein sodium salt (FSS) dye upon illumination with UV light compared with that under dark conditions to assess the effect of the oxidative stress because of the reactive oxygen species (ROS). The bare and surface modified Fe_2O_3NPs display excellent adsorption and photocatalytic activity for FSS dye. The Langmuir isotherm and the pseudo-second order kinetic model fit well with the adsorption properties of the Fe_2O_3NPs. The nanoparticles of the anionic surface (Fe_2O_3NPs/PSS) showed much lower adsorption and photocatalytic activity than the ones with a cationic surface functionality ($Fe_2O_3NPs/PSS/PAH$ and bare Fe_2O_3NPs). The impact of the Fe_2O_3NPs surface coating was discovered to be much stronger than the ROS impact because of irradiation with UV light. This indicates that the nanoparticles attachment to the FSS dye is much more important for their adsorption and photocatalytic action than the ROS generation alone. This could be explained by the poor adhesion of Fe_2O_3NPs/PSS to the FSS dye due to electrostatic repulsion. In contrast, the particle-FSS dye electrostatic adhesion in the case of cationic $Fe_2O_3NPs/PSS/PAH$ and bare Fe_2O_3NPs led to enhanced adsorption and photocatalytic action. Additionally, it was discovered that the $Fe_2O_3NPs/PSS/PAH$ and bare Fe_2O_3NPs were extremely selective for anionic FSS over cationic crystal violet (CV) dye, making it simple to separate the two dyes from aqueous solutions of dye mixtures. The data also displays that bare and surface modified Fe_2O_3NPs have good recyclability, showing that they would be an economical material with significant potential in water treatment.

Graphical abstract
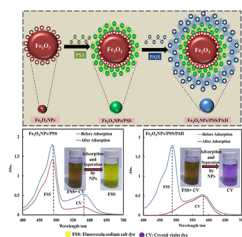
Keywords Fe_2O_3NPs · Adsorption · Photodegradation · Anionic dye · Polyelectrolytes · Selective removal

✉ Ahmed F. Halbus
   ahmed.halbus@uobabylon.edu.iq

[1] Department of Chemistry, College of Science, University of Babylon, Hilla, Iraq

Introduction

A water problem is being caused by the industry's current production of a lot of different forms of wastewater that contain dangerous chemicals [1–8]. Due to urbanization and industrialization, the world's ground water has become a severe issue. The wastewater must be treated before being released into the environment in order to avoid water pollution [9–14]. Several model organisms have been exposed to dyes, which has led to genotoxic and mutagenic effects [12, 15–17]. There are many methods used to remove dyes from wastewater including filtration, precipitation, adsorption, photodegradation, and chemical degradation [12, 18–22]. The dye compounds are classified as irritants and have adverse effects on humans, including respiratory distress, lacrimation, skin irritation, and carcinogenic consequences. The majority of synthetic dyes provide significant health risks to living systems by altering the chemical and physical properties of soil, the aquatic environment, and the flora and fauna. This causes the natural environment to collapse [23–29].

Nanotechnology has become a cutting-edge, state-of-the-art technology in recent years, with applications in every aspect of human life. Researchers have focused on creating nanoparticles and numerous techniques have been developed to achieve this goal [12, 30–35]. Finding a new solution to the problems that are now being encountered in the field of environmental technology has had an effect on people's daily lives [24, 36]. The remarkable properties of metal nanoparticles including their thermal, catalytic, mechanical, optical and magnetic capabilities, have made a scientific study of them alluring [37–41]. These distinctive characteristics are the fallout of a high surface area to volume ratio, and high surface energy contrived through nanoparticles. Metal nanoparticles are widely used in a variety of fields, including optics, electronics, material science, and the biological and medical sciences [24, 42, 43].

Iron oxide nanoparticles are getting more and more interest in the field of drug delivery and magnetic resonance imaging (MRI) because of their unique superparamagnetic properties, flexibility, low-cytotoxicity, and biocompatibility [44–47]. Many efforts are being made to produce iron oxide nanoparticles for both their vital uses across a range of fields and their fundamental scientific interest. Due to their magnetic properties, high surface area, and small size, the usage of iron oxide-based nanomaterial with unique properties and functionality is now being explored extensively [44, 48–50]. Iron oxide-based magnetic nanoparticles are used in a number of scientific, industrial, and medicinal fields [51, 52]. Nevertheless, an essential step in conjunction with such applications is the surface modification of iron oxide nanoparticles using various functionalization techniques [53–55].

Polyelectrolyte multilayers adsorbed on iron oxide nanoparticles are very significant for shielding against NPs degradation, modification of surface charge and for changing magnetization features of magnetic cores because of their interaction with polymers [56, 57]. The well-known layer-by-layer (LbL) technique, which allows for the nanoscale tailoring of the chemical and physical properties of multilayered materials, can be used to create polyelectrolyte multilayers on charged substrates [58, 59]. Additionally, the use of this technique causes a surface charge reversal [60, 61], which is determined by electrostatic interactions between the polyelectrolyte chains, solvent and substrate, which are highly influenced by factors including temperature, pH, ionic strength, and species concentration [62–64], particularly in the situation of weak polyelectrolytes like poly(allylamine hydrochloride) (PAH). Nevertheless, when the multilayer of polyelectrolyte simply involves electrostatic interactions, the rise in entropy caused by counter ion release to the bulk is the driving force for self-assembly [65, 66]. Additionally, the strong cooperatively between polymer chains (and eventually, the structure of the multilayer) will depend on the type of polymers utilized in the LbL process. In addition, the following interactions must be considered: interactions between donors and acceptors, steric interactions, hydrogen bonds, hydration interactions, covalent bonds, cycles of adsorption and drying, stereocomplex formation, or specific recognition. The surface charge of the nanoparticle is altered by these interactions, which also affects the stability of colloidal suspensions in solutions [67].

In the current study, we created iron oxide nanoparticles using the precipitation method at two calcination temperatures (200 and 500 °C). The essential benefits of the precipitation method are its high production and the low minimum temperature requirement, which prevents the formation of big grains. We also describe the production of iron oxide nanoparticles, their characterisation, and surface modifications utilizing two polyelectrolytes. Here, we investigate how the adsorption and photocatalytic activity of Fe_2O_3NPs with FSS dye is influenced by surface coatings consisting of anionic poly(sodium 4-styrenesulfonate) (PSS) and cationic poly(allylamine hydrochloride) (PAH) polyelectrolytes as shown in Fig. 1. In order to remove FSS dye from synthetic dye solutions, we investigate the photocatalytic and adsorption properties of both free Fe_2O_3NPs and surface-modified Fe_2O_3NPs. Fluorescein dye was quickly and successfully removed from an aqueous solution using surface-modified Fe_2O_3NPs. The ability of the Fe_2O_3NPs to electrostatically attach to fluorescein dye depends on the surface charge of the particles. Here, we are investigating the possibility that covering the Fe_2O_3NPs with an exterior layer of a cationic polyelectrolyte will improve their photocatalytic and adsorption activity, whereas covering them with an exterior layer of anionic polyelectrolyte may decline their photocatalytic

and adsorption activity because of electrostatic repulsion from the negatively charged fluorescein dye. The multilayer coverings offer excellent surface coverage and the external PAH layer offers superior photocatalytic and adsorption activity for fluorescein dye. To the best of our knowledge, no research has been done on the application of this type of modification for Fe_2O_3NPs made using the LbL technique and employed for the photocatalytic and adsorption of fluorescein dye. Here, we show for the first time that surface-modified Fe_2O_3NPs exhibit improved and preferred photocatalytic and adsorption activity for the FSS dye as compared to unmodified Fe_2O_3NPs.

Results and discussion

Characterization of Fe_2O_3NPs

The size and morphology of synthesized Fe_2O_3NPs were examined by TEM analysis. TEM examination was performed to get clear information about shape, size, and structural details. Figure 2A–F shows the TEM images of Fe_2O_3NPs that were produced using the precipitation method and calcined for 4 h at 200 and 500 ℃. The average particle diameter of the Fe_2O_3NPs after a 4 h heat treatment was determined to be 48 ± 10 nm at 200 ℃ (Fig. 2A–C) and 96 ± 7 nm at 500 ℃ (Fig. 2D–F). It is evident that nanoparticles are primarily found in nature as granules with small and big spherical shaped particles. The calcination temperature utilized in the synthesis of Fe_2O_3NPs has a significant impact on the nanoparticle size. The TEM images of Fe_2O_3NPs were proved that the particle size increased with the increase of the calcination temperature (Fig. 2A–F).

The BET technique was used to measure the surface areas of Fe_2O_3NPs formed from Fe_2O_3 at different temperatures. Note that the Fe_2O_3NPs surface area declined as the calcination temperature increased from 199 $m^2\ g^{-1}$ at 80 °C to 27 $m^2\ g^{-1}$ at 500 ℃ as shown in Fig. 2H. FTIR spectroscopy was used to further confirm the production of Fe_2O_3 nanoparticles. Figure 2G displays FTIR spectra of Fe_2O_3 uncalcined and calcined at 200 and 500 ℃ formed by using the precipitation method. The significant absorption peaks at 443 and 556 cm^{-1} for the uncalcined Fe_2O_3 nanoparticles product can be attributed to the vibrations of the Fe–O band [68, 69]. The very broad absorption band centered at 3398 cm^{-1} and reaching peak at 1638 cm^{-1} is attributed to the stretching and bending vibrations of the hydroxyl groups and/or water molecules, respectively [70]. The results show that the products were prepared in an aqueous solution, which resulted in the presence of structural hydroxyl groups as well as a minor quantity of absorbed water on their surface. FTIR spectrum analyses of pure Fe_2O_3 nanoparticles calcined at 200 and 500 ℃ generated by

precipitation method displays the reduction of bands related to the hydroxyl group. We also observed the appearance of two bands at 434 and 527 cm^{-1} that can be related to the Fe–O bond of Fe_2O_3NPs [71]. The characteristic peak at 434 and 527 cm^{-1} becomes very strong for Fe_2O_3 nanoparticles calcined at 200 and 500 ℃, indicating the creation of the stretching mode of Fe_2O_3. Figure S5A–C shows the Fe_2O_3NPs powder's X-ray diffraction patterns. Figure S5A displays the sample's XRD pattern before annealing, while Fig. S5B and C show the XRD pattern after annealing. The XRD results in Fig. S5A–C demonstrate that as the calcination temperature is raised, the intensity and half-height breadth of the diffraction peak steadily decrease, resulting in an increase in crystal size. Using the Scherrer equation, the range of average crystallite sizes found in the XRD data was 4–16 nm. It was discovered as a result that altering the calcination temperature resulted in a change in the crystallite size of pure Fe_2O_3NPs. An Energy Dispersive X-ray Diffraction (EDX) analysis was also carried out to confirm the elemental composition of the generated Fe_2O_3NPs. It was found that the iron and oxygen signals are present in the Fe_2O_3NPs sample, according to the EDX results in Fig. S5D.

To study the formation of each polyelectrolyte layer deposited on the Fe_2O_3NPs, the zeta potential and hydrodynamic diameter experiments were measured by DLS. We coated two additional layers of PSS and PAH to cover Fe_2O_3NPs that were 70 nm at 200 ℃ and 95 nm at 500 ℃ using the methods described above [33, 64]. Figure 3A, B displays that the coated Fe_2O_3NPs size increases after each additional polyelectrolyte coating because of partial aggregation. The variation of zeta potential with the polyelectrolyte layer number for PSS and PAH coatings are presented in Fig. 3C, D. The zeta potential of the Fe_2O_3NPs changed from a positive charge to a negative charge for Fe_2O_3NPs/PSS due to PSS single layer being a negatively charged. An additional PAH coating produced positively charged Fe_2O_3NPs/PSS/PAH with zeta potentials of $+42$ mV (Fig. 3C) and $+31$ mV (Fig. 3D). Adding the polyelectrolyte layer with the opposing charge causes the particle surface charge to alternate, as expected.

FSS dye adsorption and photocatalytic studies

#### The effect of the amount of Fe_2O_3NPs on FSS dye adsorption

We investigated the photocatalytic and adsorption properties of Fe_2O_3NPs toward FSS dye under UV irradiation as well as in dark conditions. Different Fe_2O_3NPs adsorbent amounts including 0.05 g, 0.1 g, 0.15 g, 0.2 g, 0.25 g, and 0.3 g were utilized to evaluate the effects of nanoparticle amounts calcined at 200 and 500 ℃ in the removal of FSS dye. The works were carried out in 100 cm^3 solution of
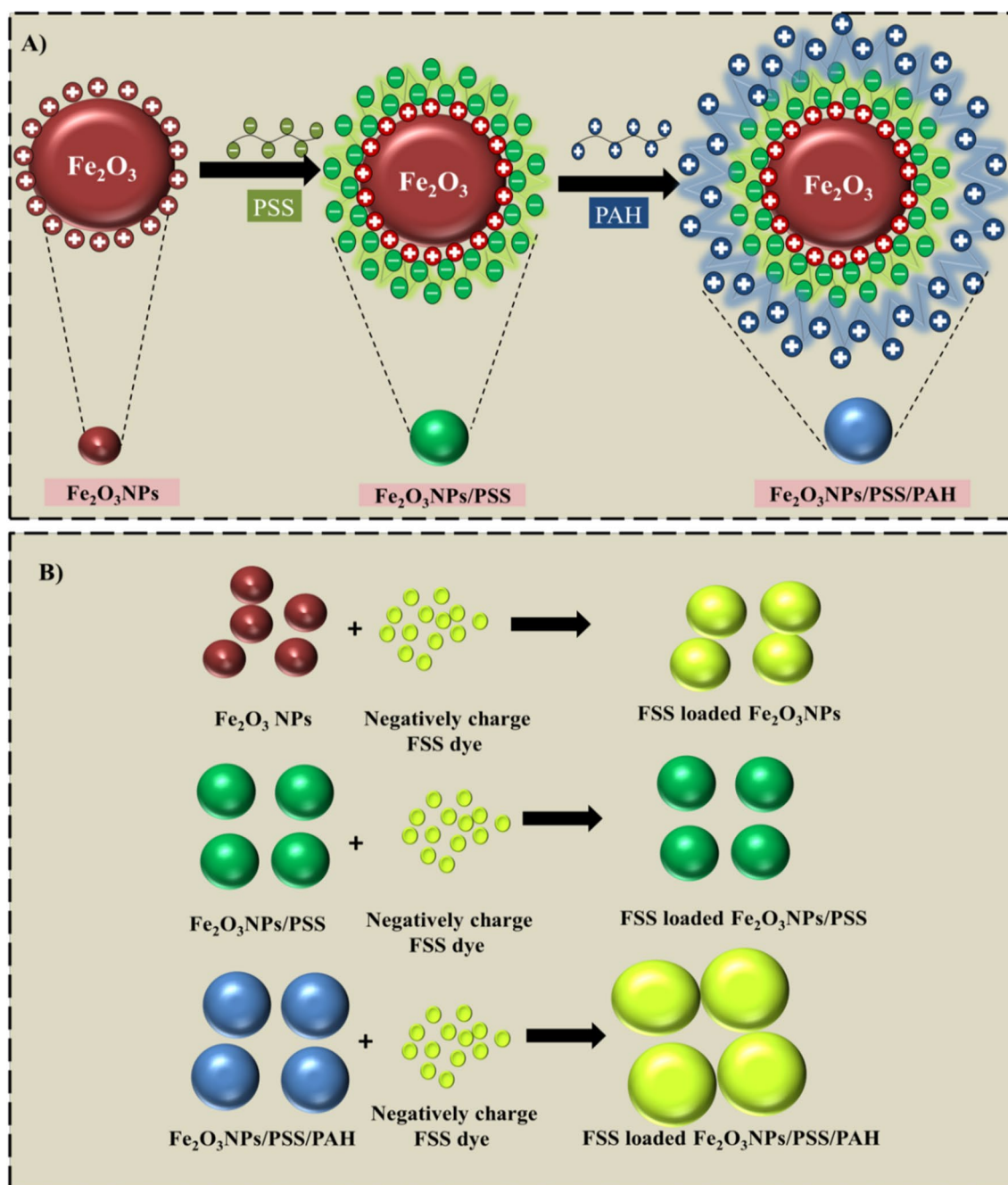
Fig. 1 **A** Schematic diagram showing the coating of bare Fe$_2$O$_3$NPs with two consecutive layers of anionic PSS and cationic PAH polyelectrolytes. **B** Schematic diagram showing the adsorption of FSS dye on bare and surface modified Fe$_2$O$_3$NPs

10 mg dm^{-3} initial FSS concentration at room temperature. The percentage of FSS dye adsorption and photodegradation efficiency increased with increasing doses of Fe$_2$O$_3$NPs as illustrated in Fig. 4 and Fig. S3. This was explained by the fact that as the amount of adsorbent increases, there is a higher chance that the FSS dye will come into touch with the available active sites of the Fe$_2$O$_3$NPs. As an anionic dye model, FSS dye was used in the present research

to evaluate how well Fe$_2$O$_3$NPs removed FSS dyes in both dark and light conditions. This result could be attributed to the anionic dye being electrostatically attracted to cationic Fe$_2$O$_3$NPs, which causes the FSS dye to be absorbed by Fe$_2$O$_3$NPs. After adsorption of 0.05 g of Fe$_2$O$_3$NPs with 10 mg dm^{-3} of FSS dye, there was a noticeable difference in FSS dye removal in dark (Fig. 4C and Fig. S3C) and UV light conditions (Fig. 4D and Fig. S3D) because of the
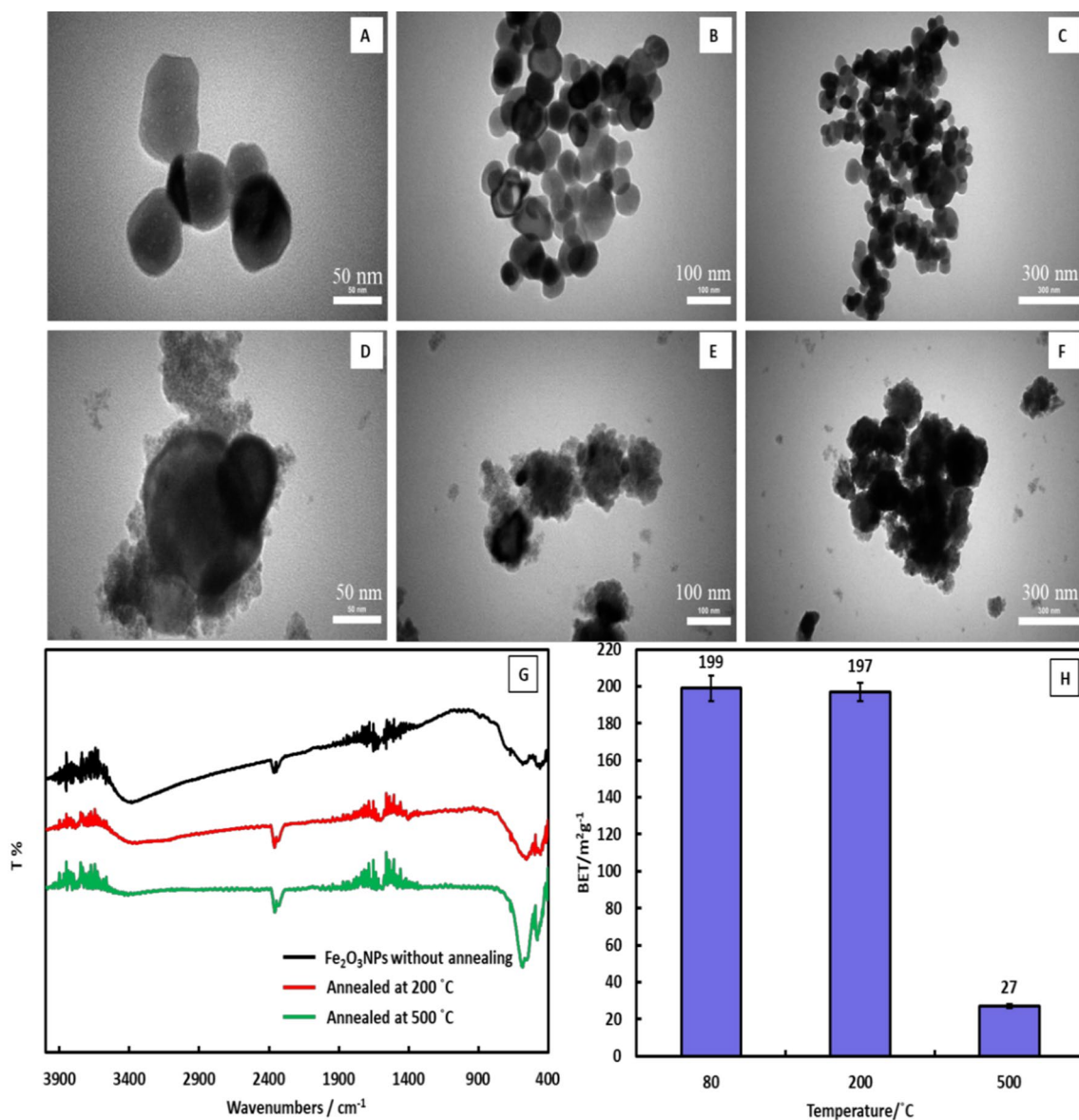
Fig. 2 TEM images of Fe_2O_3NPs at lower and higher magnifications prepared with different calcination temperatures. **A–C** calcined at 200 ℃ and **D–F** calcined at 500 ℃. **G** FTIR spectrum of Fe_2O_3 uncalcined and calcined at 200 and 500 ℃ produced by precipitation method. **H** The impact of the calcination temperature during the Fe_2O_3NPs synthesis on the BET surface area of Fe_2O_3NPs from 80 to 500 ℃

photoactivity of the Fe_2O_3NPs. FSS dye quickly adsorbs to Fe_2O_3NPs at first, but the adsorption activity gradually slows and reaches equilibrium after 10 min under UV light and darkness, as illustrated in Fig. 4 and Fig. S3. The rate of adsorption varies quickly since all of the adsorbent sites are initially empty. The decrease in the number of unoccupied adsorbent sites and the dye concentration over time cause the adsorption rate to become low. The decreased rate of adsorption indicates that FSS probably formed a monolayer on the surface of the Fe_2O_3NPs. As a consequence, once equilibrium is reached, there aren't enough free active sites, therefore more absorption is required. The removal percentage

of FSS dye that was adsorbed by Fe_2O_3NPs calcined at 200 and 500 ℃ in both light and dark was reported. Figure 4 and Fig. S3 show that the removal percentage of FSS dyes using Fe_2O_3NPs under UV light is higher than that in the dark at the same conditions. One probable description is that aqueous suspensions of Fe_2O_3NPs under UV light can produce ROS like $O_2^{\bullet-}$ and H_2O_2 [64]. The decolorization of dyes is widely discussed in the literature review. The hydroxyl radicals are generated in a solution that acts as an oxidant, which is formed on Fe_2O_3NPs. Furthermore, when water molecules on the surface of Fe_2O_3NPs interact with holes ($h^+_{(VB)}$), hydroxyl ion radicals are generated. Therefore,

hydroxyl ion radicals destroy the FSS dye [17, 27]. The results represented in Fig. S3 show that the Fe_2O_3NPs calcined at 500 ℃ have lower adsorption and photocatalytic activity on FSS dye when compared to the Fe_2O_3NPs calcined at 200 ℃ (Fig. 4). One possible explanation is that the increase of the calcination temperature leads to an increase of size of Fe_2O_3NPs. Thus, the smallest size was obtained at the lowest calcination temperature (200 ℃). It was also found that the Fe_2O_3NPs surface area increased as the calcination temperature declined as described above.

Effect of initial FSS dye concentration

One of the most significant aspects affecting the adsorption process may be the initial dye concentration since it indirectly impacts the effectiveness of dye removal by lowering

or raising the number of binding sites on the adsorbent surface. The effectiveness of dye removal and the maximum amount of dye bound in equilibrium in such systems of water treatment are strongly related to the initial dye concentration [72]. By changing the initial concentration of the FSS dye over a wide range (5–50 mg dm^{-3}), the impact of the initial concentration on the removal percentage and photodegradation efficiency was examined. Adsorption and photocatalytic tests were conducted at various initial FSS dye concentrations of FSS dye at a fixed pH and 0.2 g of Fe_2O_3NPs. The results in Fig. 5 and Fig. S4 show that the removal percentage and photodegradation efficiency of FSS dye decreased with increasing the initial FSS dye concentration. The saturation of adsorption sites on the adsorbent surface can explain for this phenomenon. In this situation, as the initial FSS dye concentration increases, so does the ability of the adsorbent, which is because of the high mass transfer driving force at high initial FSS concentrations. The
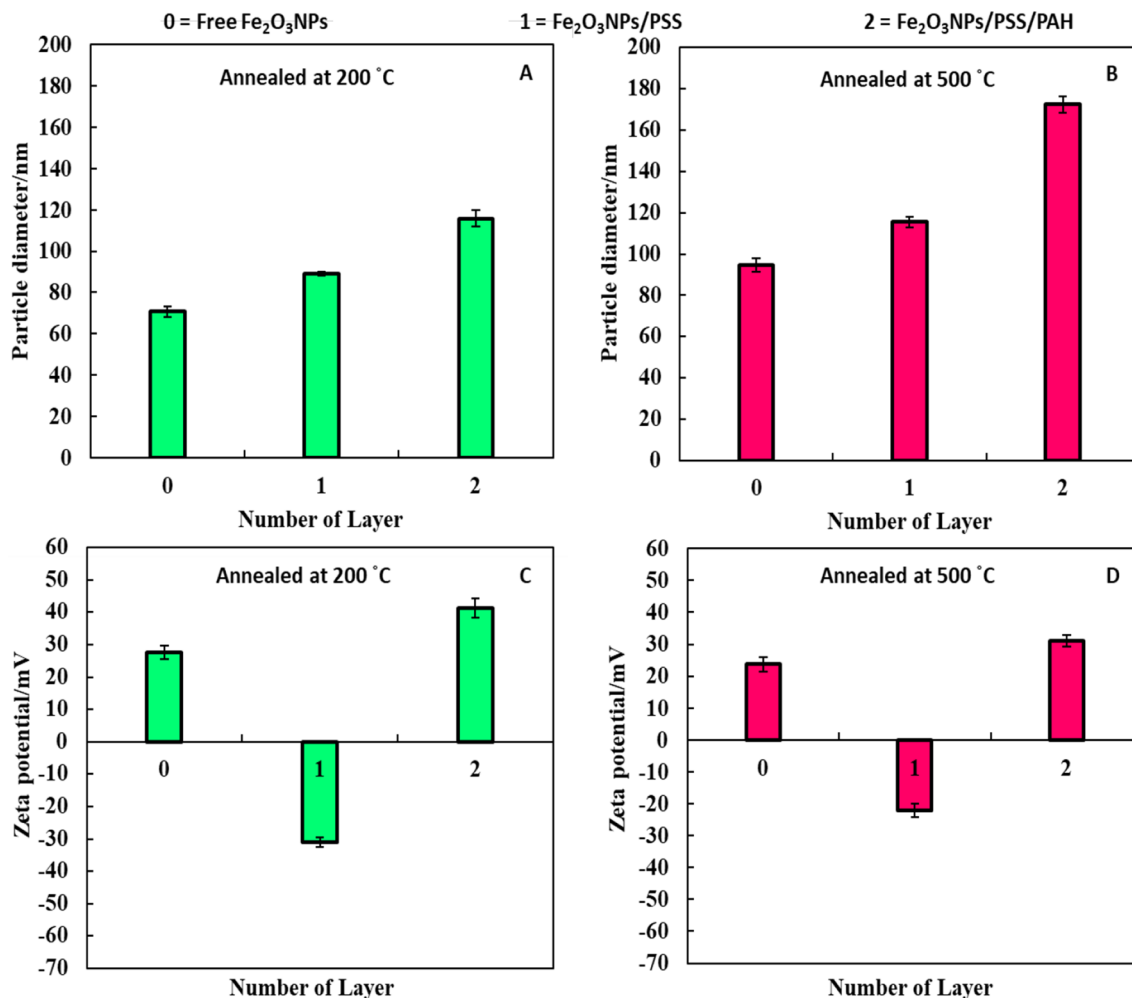

Fig. 3 **A** and **B** The particle size and **C** and **D** zeta potential of bare- and polymer-modified Fe_2O_3NPs calcined at 200 and 500 ℃ as a function of PSS and PAH layers. The free Fe_2O_3NPs are represented by the zero layers. PSS deposition is represented by layer number 1 and PAH deposition is represented by layer number 2

initial FSS dye concentration of the solute drives the adsorption process by favoring mass transfer and diffusion from the solution (which contains a higher amount of FSS dye) to the adsorbent's free surface [72]. At higher initial FSS dye concentrations, the total free adsorption sites are limited, which could result in a decrease in the removal percentage of FSS dye. The rise at higher initial FSS dye concentrations could be attributed to increased driving forces. On the other hand, because the ratio of active sites to FSS dye molecules can be high at low concentrations, all molecules can interact with the adsorbent and are nearly immediately removed from the solution [72]. We also examined the adsorption and photocatalytic activity of bare Fe_2O_3NPs toward various concentrations of FSS dye upon illumination with UV light compared with that under dark conditions to assess the influence of the oxidative stress owing to the reactive oxygen species (ROS). The data in Fig. 5 and Fig. S4 show

that there was a remarkable difference between the removal percentage of FSS dye in dark conditions (Fig. 5C) and that under UV light (Fig. 5D) because of the photoactivity of the Fe_2O_3NPs. One possible explanation is that under UV irradiation, electrons in the VB may be stimulated to the CB of the oxide, with the concomitant creation of the same quantity of holes in the VB, resulting in the creation of an electron–hole pair. Redox reactions with organics can then result from further charge separation and the migration of the created charge carriers toward the surface of the catalyst. In terms of redox potentials, reducing the fluorescent dye can occur at potential ($E^0 \approx -0.34$ V vs. Ag/AgCl). On another hand, the valence band of iron oxide is located at 2.5 V and its conduction band is located at 0.4 V, this means that it is comparable to the reduction of FSS by CB of iron oxide [73]. Direct oxidation of the FSS dye to reactive intermediates is possible due to the high oxidative potential of
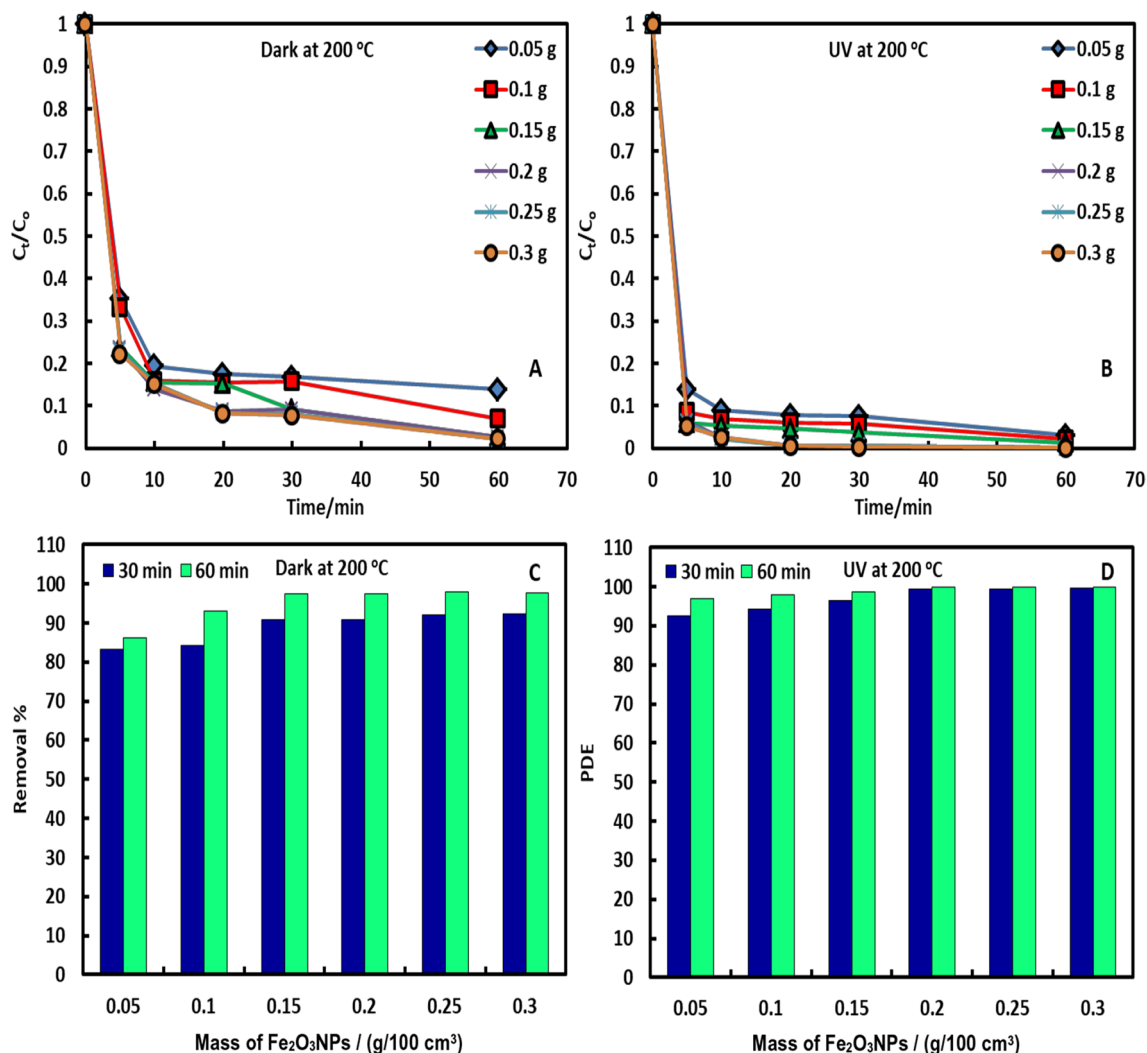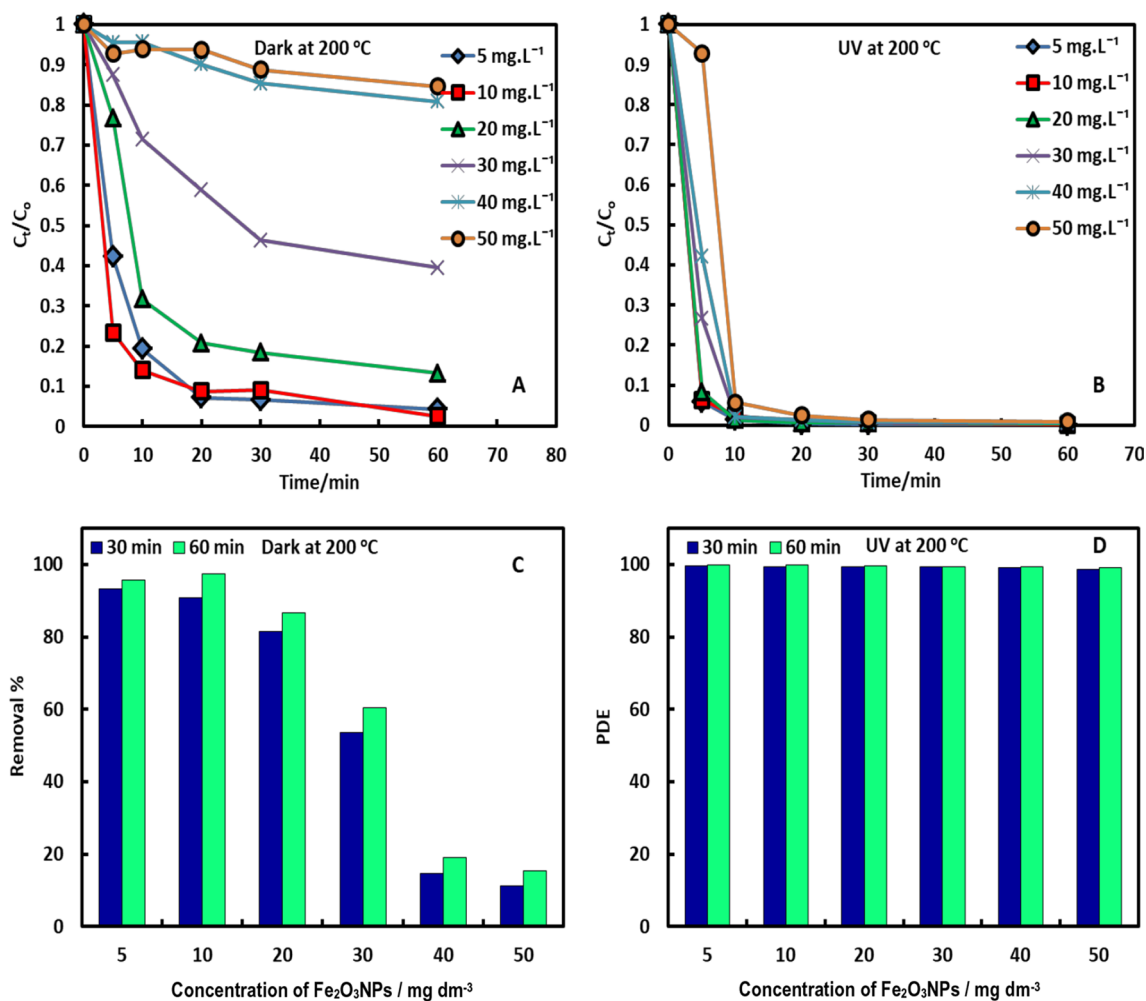

Fig. 4 The impact of Fe_2O_3NPs amount calcined at 200 ℃ on the removal percentage and photodegradation efficiency of FSS dye under (**A** and **C**) dark conditions and (**B** and **D**) UV light

the hole (h^+) (VB) in the Fe_2O_3NPs. Another way that water might decompose is to produce hydroxyl radicals, which are extremely reactive. On the other hand, a more effective reaction will occur when electrons interact with dissolved oxygen molecules to form superoxide radical anions, which then protonate to become hydroperoxyl radicals ($HO_2^\bullet$) and lastly $OH^\bullet$ radicals [71].

Kinetics and adsorption isotherms of FSS dye adsorption on Fe_2O_3NPs

The kinetics of FSS adsorption on Fe_2O_3NPs was studied. At room temperature, batch systems were used for all experimental tests. Kinetic studies are crucial in the field of adsorption because they shed light on the adsorption mechanism. The adsorption ability and rate constant of a Fe_2O_3NPs substance used as an adsorbent must be higher. In this work, pseudo-first- and second-order kinetics was used. The perfectly matched plots of the adsorption kinetic model are shown in Fig. 6A, B. First-order kinetic graphs for the FSS dye are shown in Fig. 6A, whereas second-order kinetic plots are shown in Fig. 6B. We discovered that the correlation coefficient of the pseudo-second-order model was significantly higher than that of the pseudo-first-order model (Table S1). Additionally, it was observed that the pseudo-second-order model's plotted simulated adsorption capacity had a better fit with the data than the pseudo-first-order model's estimated adsorption capacity (see Fig. 6A, B). Thus, the pseudo-second-order model provides the most accurate description of the adsorption mechanism for FSS dye on Fe_2O_3NPs. The kinetic parameters for FSS dye on Fe_2O_3NPs obtained from the plots in Fig. 6A, B are given in Table S1. The interaction between adsorbate particles and adsorbents can be predicted using the isotherm models, which offer useful information. Applying the Langmuir and Freundlich linear isotherm models, the mechanism of FSS

Fig. 5 Effect of initial concentration on the removal percentage and photodegradation efficiency of FSS dye under (**A** and **C**) dark conditions and (**B** and **D**) UV light in the presence of Fe_2O_3NPs calcined at 200 ℃

dye adsorption onto Fe_2O_3NPs was investigated. Figure 6C displays the Langmuir isotherms of FSS dye on Fe_2O_3NPs, whereas Fig. 6D displays the Freundlich isotherm models. These models were used to determine the maximum adsorption abilities of FSS dye on Fe_2O_3NPs. It was found that adsorption isotherms of FSS dye adsorption on Fe_2O_3NPs show good agreement with the Langmuir isotherm model. We use the calculated n values of the Freundlich model to illustrate the heterogeneities on the surface of Fe_2O_3NPs (Fig. 6D). In cases where n is more than 1, equal to 1, or less than 1, adsorption will be physical, linear, or chemical, respectively. The FSS dye has n values higher than 1 as shown in Fig. 6E, which in our study suggests that the absorption is physical absorption [17].

Adsorption and photocatalytic activity of polyelectrolyte-coated Fe_2O_3NPs toward FSS dye

We studied the adsorption and photocatalytic activity of Fe_2O_3NPs that were coated with multilayers of polyelectrolytes on FSS dye. We functionalized Fe_2O_3NPs with PSS and PAH and compared their FSS dye removal percentage and photodegradation efficiency with that of the bare Fe_2O_3NPs in dark and UV light. The aqueous solution of 10 mg dm^{-3} FSS dye were mixed with 0.2 g of Fe_2O_3NPs/PSS and Fe_2O_3NPs/PSS/PAH suspensions at various time for up to one hour. The results represented in Figs. 7A, C and 8A, C show that the anionic Fe_2O_3NPs/PSS have a lower adsorption and photocatalytic activity toward FSS dye when compared to the cationic bare Fe_2O_3NPs (see Fig. 4). The same treatment with the cationic Fe2O3NPs/PSS/PAH showed significant adsorption and photocatalytic activity toward FSS dye as shown in Figs. 7B, D and 8B, D. One can conclude that, by coating the Fe2O3NPs with an outer layer of anionic polyelectrolyte, their removal percentage and photodegradation efficiency is significantly decreased because of the electrostatic repulsion between the anionic Fe_2O_3NPs/PSS and the anionic surface of FSS dye. On the other hand, after coating Fe_2O_3NPs/PSS with an additional layer of PAH which reverses the particles surface charge from negative to positive. The positive surface charge of the Fe_2O_3NPs/PSS/PAH had a high influence on the removal percentage and photodegradation efficiency of FSS dye. The results indicate that these cationic nanoparticles Fe_2O_3NPs/PSS/PAH were even more effective for the removal of FSS dye than the bare Fe_2O_3NPs both under UV light and dark as shown in Figs. 7B, D and 8B, D. This formula of alternating adsorption and photocatalytic activity of the polyelectrolyte-coated Fe_2O_3NPs seems to be linked to their surface charge and the corresponding electrostatic adhesion to the negatively charged FSS dye. The data display that the cationic nanoparticles (the free Fe_2O_3NPs and Fe_2O_3NPs/PSS/PAH)

have much higher removal percentage and photodegradation efficiency than their anionic form Fe_2O_3NPs/PSS.

Figure 9A–D summarizes the effect of free PSS, free PAH, bare Fe_2O_3NPs, Fe_2O_3NPs/PSS, and Fe_2O_3NPs/PSS/PAH on the removal percentage and photodegradation efficiency of 10 mg dm^{-3} FSS dye under the same conditions of 0.2 g particle dose for 1 h in dark and UV light. This result indicated that the bare Fe_2O_3NPs and Fe_2O_3NPs/PSS/PAH have a strong effect on the removal of FSS dye both in dark and under UV light. This influence can be described with the positive particle surface charge leading to a strong electrostatic attraction between the cationic surface of the bare Fe_2O_3NPs and Fe_2O_3NPs/PSS/PAH and the anionic surface of the FSS dye. The data in Fig. 9A, C, D show that the presence of Fe_2O_3NPs/PSS/PAH has a much higher impact on the FSS dye removal percentage in dark, and UV light conditions than that of the bare Fe_2O_3NPs, as the adhesion of the latter to the FSS dye is driven mainly by electrostatic forces. The results confirm that free PSS and free PAH on FSS dye have a negligible adsorption and photocatalytic activity on the FSS dye, whereas Fe_2O_3NPs/PSS have some low level of effect compared with the uncoated Fe_2O_3NPs and Fe_2O_3NPs/PSS/PAH. This is most likely due to the electrostatic repulsion between Fe_2O_3NPs/PSS and FSS dye as both have negatively charged surfaces in aqueous media which leads to a decrease in the removal percentage and photodegradation efficiency of FSS dye on Fe_2O_3NPs/PSS.

We also investigated the adsorption of Reactive Red 2 dyes (RR2) as a real pollutant dye on free Fe_2O_3NPs and polyelectrolyte-coated Fe_2O_3NPs. In order to evaluate the RR2 dye removal% of free Fe_2O_3NPs and Fe_2O_3NPs functionalized with PSS and PAH were used. The aqueous solution of 70 mg dm^{-3} RR2 dye were mixed with 0.2 g of Fe_2O_3NPs, Fe_2O_3NPs/PSS and Fe_2O_3NPs/PSS/PAH suspensions at various time for up to 1 h. The data in Figs. S7 and S9 (Supporting Information) demonstrate that the anionic Fe_2O_3NPs/PSS has lower adsorption for the RR2 dye than the cationic bare Fe_2O_3NPs (see Fig. S6). The same treatment with the cationic Fe_2O_3NPs/PSS/PAH displayed significant adsorption with RR2 dye as presented in Figs. S8 and S9. According to the results in Figs. S8 and S9, it was found the cationic nanoparticles Fe_2O_3NPs/PSS/PAH were even more effective at removing RR2 dye than bare Fe_2O_3NPs and anionic Fe_2O_3NPs/PSS.

Separation of a mixture of dyes

Bare and surface modified Fe_2O_3NPs were employed to selectively separate different organic dyes because of their distinct and quick adsorption action towards FSS dye. The separation performance of unmodified and surface-modified Fe_2O_3NPs was tested using FSS/crystal violet (CV) dye mixtures in an aqueous solution with various charge states.
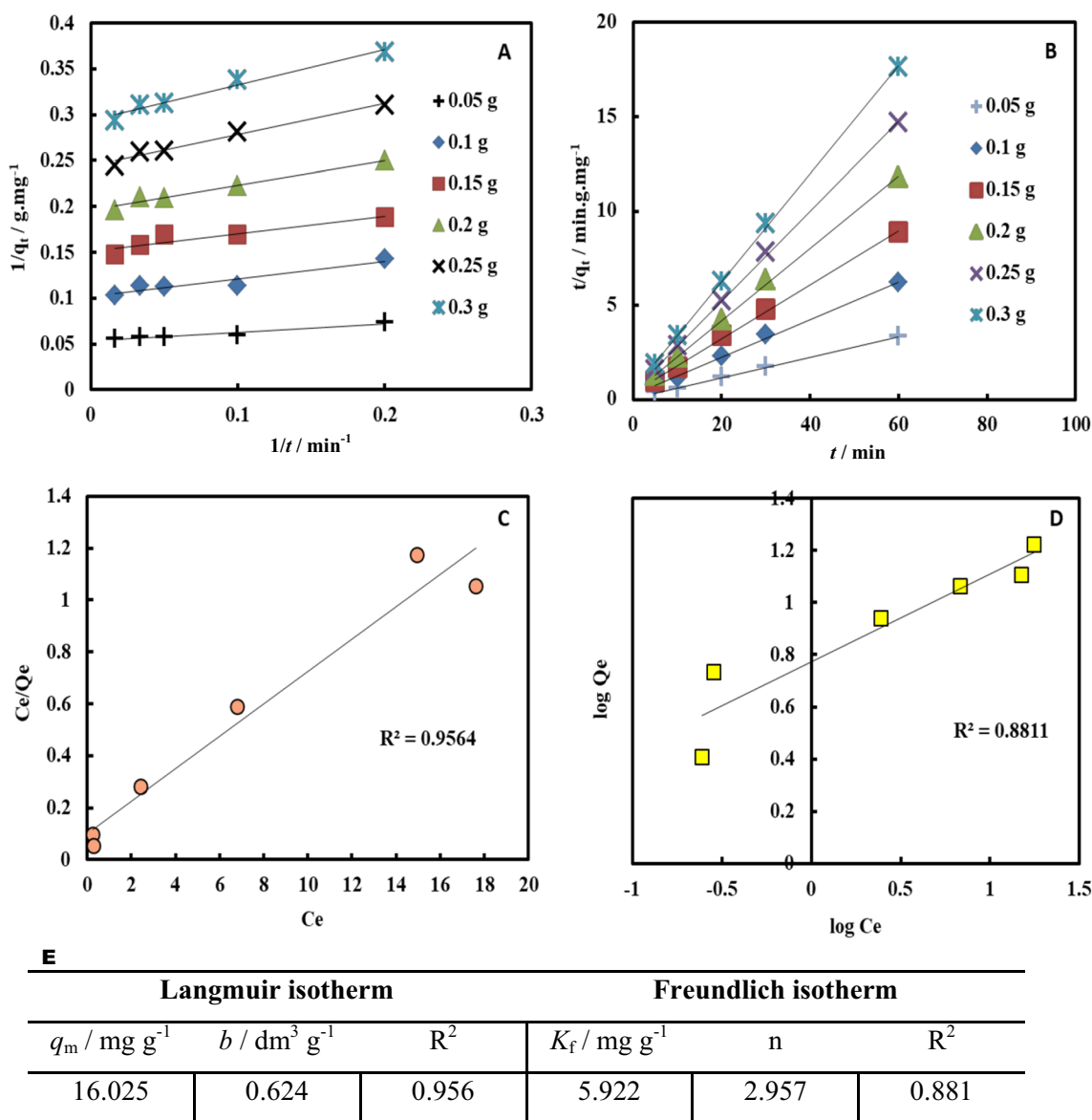
Fig. 6 Kinetics and adsorption isotherms of FSS dye adsorption on Fe₂O₃NPs. **A** Pseudo-first-order model and **B** pseudo-second-order model for FSS dye. Adsorption isotherms for FSS dye on Fe₂O₃NPs according to **C** Langmuir and **D** Freundlich isotherm models

Free Fe_2O_3NPs and Fe_2O_3NPs/PSS/PAH are designed to eliminate anionic FSS dye from the mixed solution, whilst Fe_2O_3NPs/PSS may be able to remove cationic CV dye. Digital photos of the dye mixture of FSS and CV before and after adsorption with free Fe_2O_3NPs, Fe_2O_3NPs/PSS, and Fe_2O_3NPs/PSS/PAH were taken, as shown in Fig. 10B, D, F. The colors of the dye mixture were then compared to those of the two separate (Fig. 10A) aqueous solutions of FSS/CV dyes. The color of the mixture of yellow FSS and blue-violet CV dyes changed to brown after being mixed as shown in Fig. 10A. The dye mixture solution's color changed from brown to blue-violet after 1 h of adsorption, fitting the color of the pure CV aqueous solution (Fig. 10B, F).

Nearly all of the FSS dye was absorbed by the Fe_2O_3NPs and Fe_2O_3NPs/PSS/PAH (Fig. 10C, G). On the other hand, the Fe_2O_3NPs/PSS effectively absorbed all of the CV dyes (Fig. 10E), changing the color of the dye combination solution from brown to yellow (Fig. 10D), which matched the color of the pure FSS aqueous solution. The concentrations of FSS and CV in the mixture solution were determined using UV–Vis spectra before and after 1 h of adsorption with unmodified and surface-modified Fe_2O_3NPs, as shown in Fig. 10B, D, F. According to UV–Vis spectra measured after 1 h, Fe_2O_3NPs and Fe_2O_3NPs/PSS/PAH absorbed between 85 and 98% of the FSS, whereas only a mere 10% of the CV. This demonstrates that the dye mixture can be
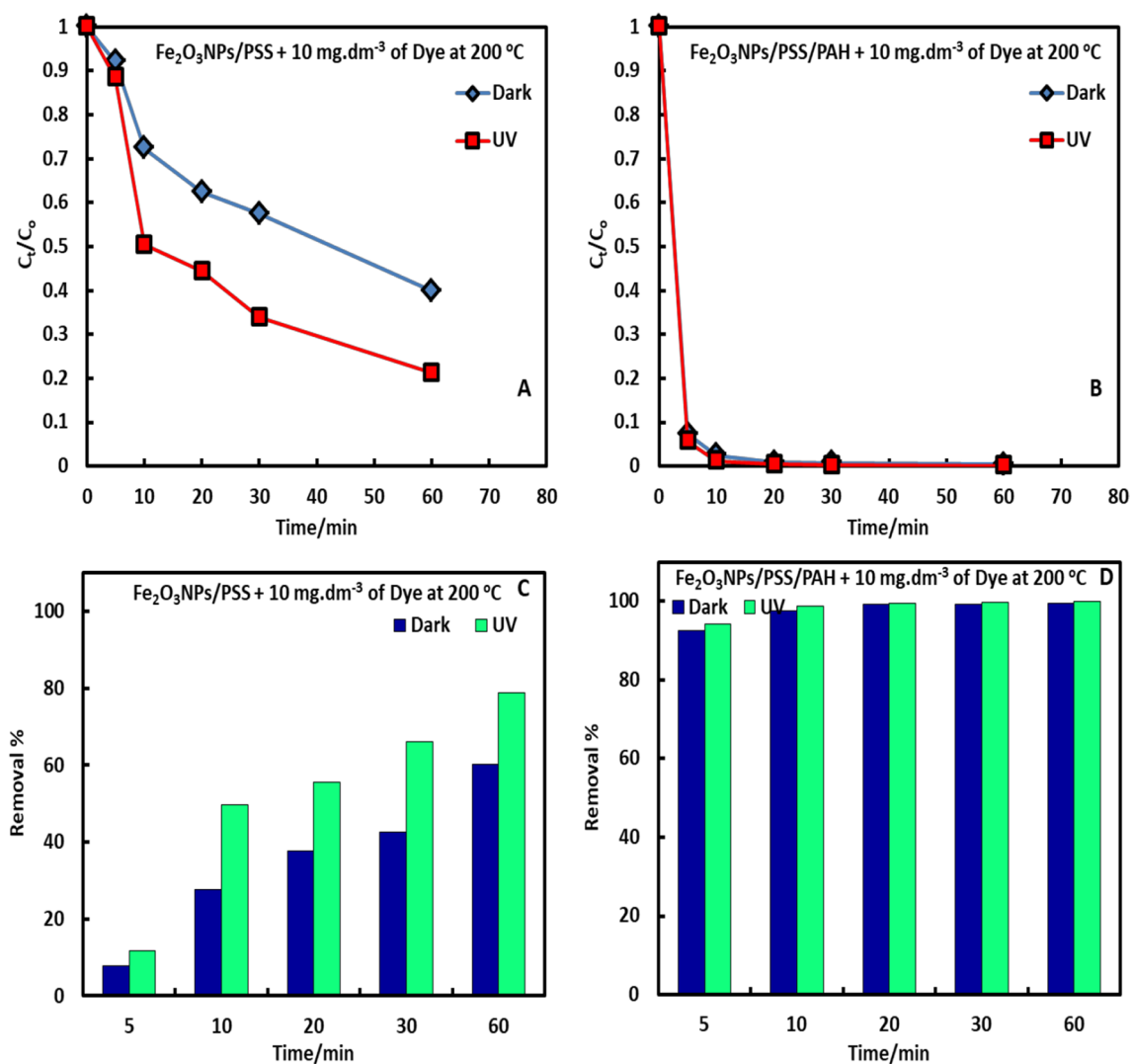
Fig. 7 The removal percentage and photodegradation efficiency of FSS dye on polyelectrolyte-coated Fe_2O_3NPs synthesized after anneali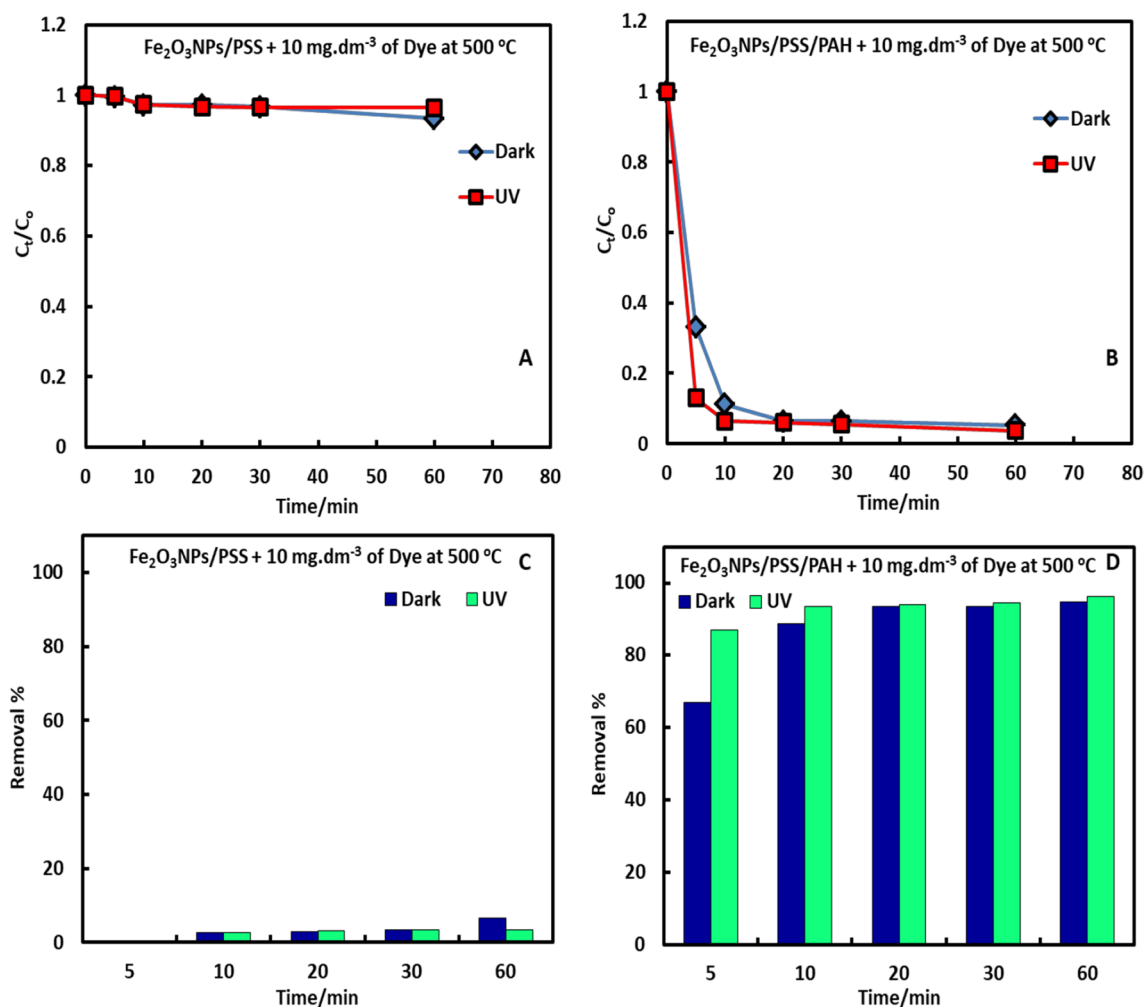ng of Fe_2O_3 at 200 ℃ toward FSS dye. The removal percentage of 10 mg dm^{-3} FSS dyes after mixing for up to 1 h with **A, C** 0.2 g of Fe_2O_3NPs/PSS and **B, D** Fe_2O_3NPs/PSS/PAH at room temperature

successfully separated using Fe_2O_3NPs and Fe_2O_3NPs/PSS/PAH by selectively adsorbing FSS from the dye mixture. These results can be explained by the reduced adsorption Fe_2O_3NPs and Fe_2O_3NPs/PSS/PAH to the CV dye because of electrostatic repulsion and the better particle-dye adsorption due to electrostatic interaction when cationic Fe_2O_3NPs and Fe_2O_3NPs/PSS/PAH are combined with anionic FSS dye.

Regeneration and reuse of used bare and surface modified Fe_2O_3NPs

In practical applications, an adsorbent's ability to be reused sustainably is important. As a result, the reuse and regeneration of the utilized Fe_2O_3NPs, Fe_2O_3NPs/PSS, and

Fe_2O_3NPs/PSS/PAH were also assessed for 5 cycles adsorption/desorption and the results are displayed in Fig. 11A. The desorption of FSS dye was achieved by putting the loaded FSS-nanoparticles for 3 h in 0.01 N NaOH, followed by washing five times with deionized water as shown in Fig. 11B–G. The electrostatic attraction between the Fe_2O_3NPs and Fe_2O_3NPs/PSS/PAH and the anionic FSS dye was decreased as expected as a result of deprotonating. Fe_2O_3NPs and Fe_2O_3NPs/PSS/PAH show high removal efficiency after five cycles of adsorption–desorption. As the number of reuse cycles increased, the FSS dye removal effectiveness declined; nonetheless, both the unmodified and surface-modified Fe_2O_3NPs lost approximately 5% of their initial efficiency over the course of five cycles. Consequently, the decline in removal effectiveness may be brought

Fig. 8 The removal percentage and photodegradation efficiency of FSS dye on polyelectrolyte-coated Fe_2O_3NPs synthesized after annealing of Fe_2O_3 at 500 ℃ toward FSS dye. The removal percentage of 10 mg dm^{-3} FSS dyes after mixing for up to 1 h with **A**, **C** 0.2 g of Fe_2O_3NPs/PSS and **B**, **D** $Fe_2O_3NPs/PSS/PAH$ at room temperature

on by the changing of the surface properties of the unmodified and surface-modified Fe_2O_3NPs throughout the adsorption–desorption processes [17]. These results demonstrate that both the uncoated and surface-coated Fe_2O_3NPs are highly recyclable, making them an economical material with promising water treatment applications.

Conclusion

Here we explored and discussed the mechanisms by which bare and surface modified Fe_2O_3NPs attack FSS dye. In this study, we used the precipitation method to produce Fe_2O_3NPs at two calcination temperatures (200 and 500 ℃). The effects of changes in the calcination temperature used in the synthesis of Fe_2O_3NPs at the level of size and morphology were discovered. TEM, FTIR, BET, and DLS techniques

were used to characterize the synthesized Fe_2O_3NPs. The data of the various techniques display that the increase of the calcination temperature leads to an increase of size of Fe_2O_3NPs. In summary, the lowest calcination temperature (200 ℃) resulted in the smallest size (48 nm). The adsorption of FSS dye onto bare and surface modified Fe_2O_3NPs and its photocatalytic activity were then studied. Our present work indicates that bare Fe_2O_3NPs had significant adsorption and photocatalytic activity against FSS dye and their impact increased upon increasing the Fe_2O_3NPs dose. To analyze the adsorption process, the kinetics of FSS dye adsorption was investigated. The results showed that the kinetic data worked well with the pseudo-second-order kinetic model. The Langmuir isotherm model was found to best fit the adsorption equilibrium results for FSS dye adsorption. To evaluate the influence of the surface coating, a series of Fe_2O_3NPs coated with polyelectrolytes using the layer
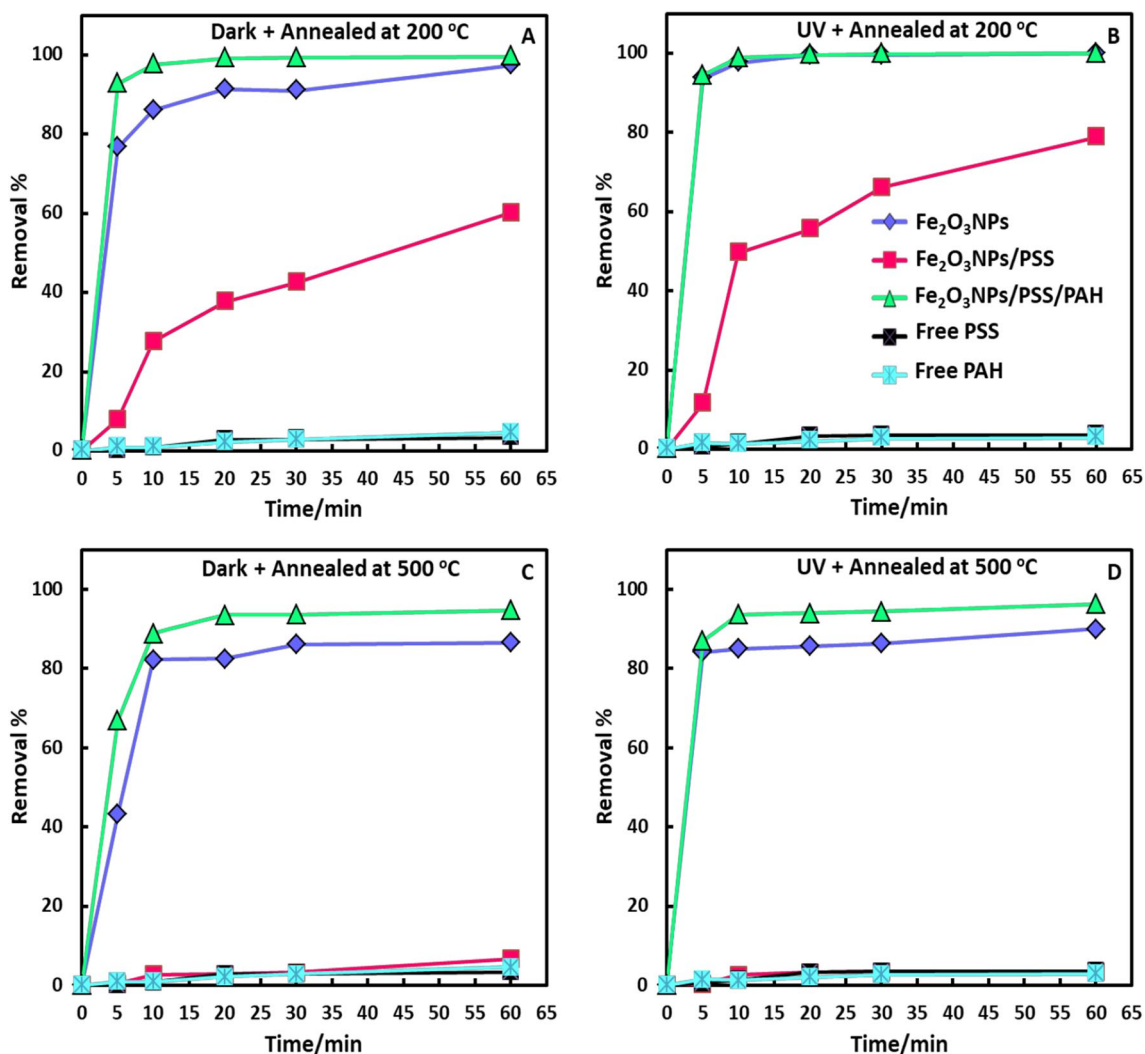
Fig. 9 Comparison of the effect of free PSS, free PAH, free Fe$_2$O$_3$NPs, Fe$_2$O$_3$NPs/PSS, and Fe$_2$O$_3$NPs/PSS/PAH on the removal percentage and photodegradation efficiency of FSS dye in **A**, **C** dark and **B**, **D** UV light for 1 h. 10 mg dm^{-3} of FSS dye was mixed with the 0.2 g of nanoparticles synthesized after annealing of Fe$_2$O$_3$ at **A**, **B** 200 ℃ and **C**, **D** 500 ℃

by-layer technique were synthesized and their adsorption and photocatalytic activity toward FSS dye was compared to that of the bare Fe$_2$O$_3$NPs. It was discovered that the adsorption and photocatalytic activity of the surface-modified Fe$_2$O$_3$NPs alternates with the particle surface charge. The nanoparticles of anionic surface (Fe$_2$O$_3$NPs/PSS) had much lower adsorption and photocatalytic activity than the ones of cationic surfaces (Fe$_2$O$_3$NPs/PSS/PAH and bare Fe$_2$O$_3$NPs). In general, free Fe$_2$O$_3$NPs and Fe$_2$O$_3$NPs/PSS/PAH showed remarkable adsorption and photocatalytic activity and demonstrated high efficiency against the FSS dye, even at low particle amounts. It has been observed that small amounts of cationic nanoparticles (Fe$_2$O$_3$NPs/PSS/PAH and bare Fe$_2$O$_3$NPs) have been found to remove FSS dye with efficiencies greater than 95%. This effect can be explained by the positive surface charge of the particles, which causes a

strong electrostatic attraction between the anionic surface of the FSS dye and the cationic surface of the bare Fe$_2$O$_3$NPs and Fe$_2$O$_3$NPs/PSS/PAH. Our results provide new insights about the influence of the Fe$_2$O$_3$NPs surface coatings with polyelectrolytes using the layer by-layer technique on their adsorption and photocatalytic action and could potentially lead to development of better adsorption and photocatalytic activity formulations. It was also found that the anionic FSS dye has much higher adsorbed selectively on the Fe$_2$O$_3$NPs/PSS/PAH and free Fe$_2$O$_3$NPs adsorbent than the cationic ones. The study also showed that bare and surface modified Fe$_2$O$_3$NPs presented high recyclability performance and thus they will be low-cost materials and have superior probability in the treatment of water.
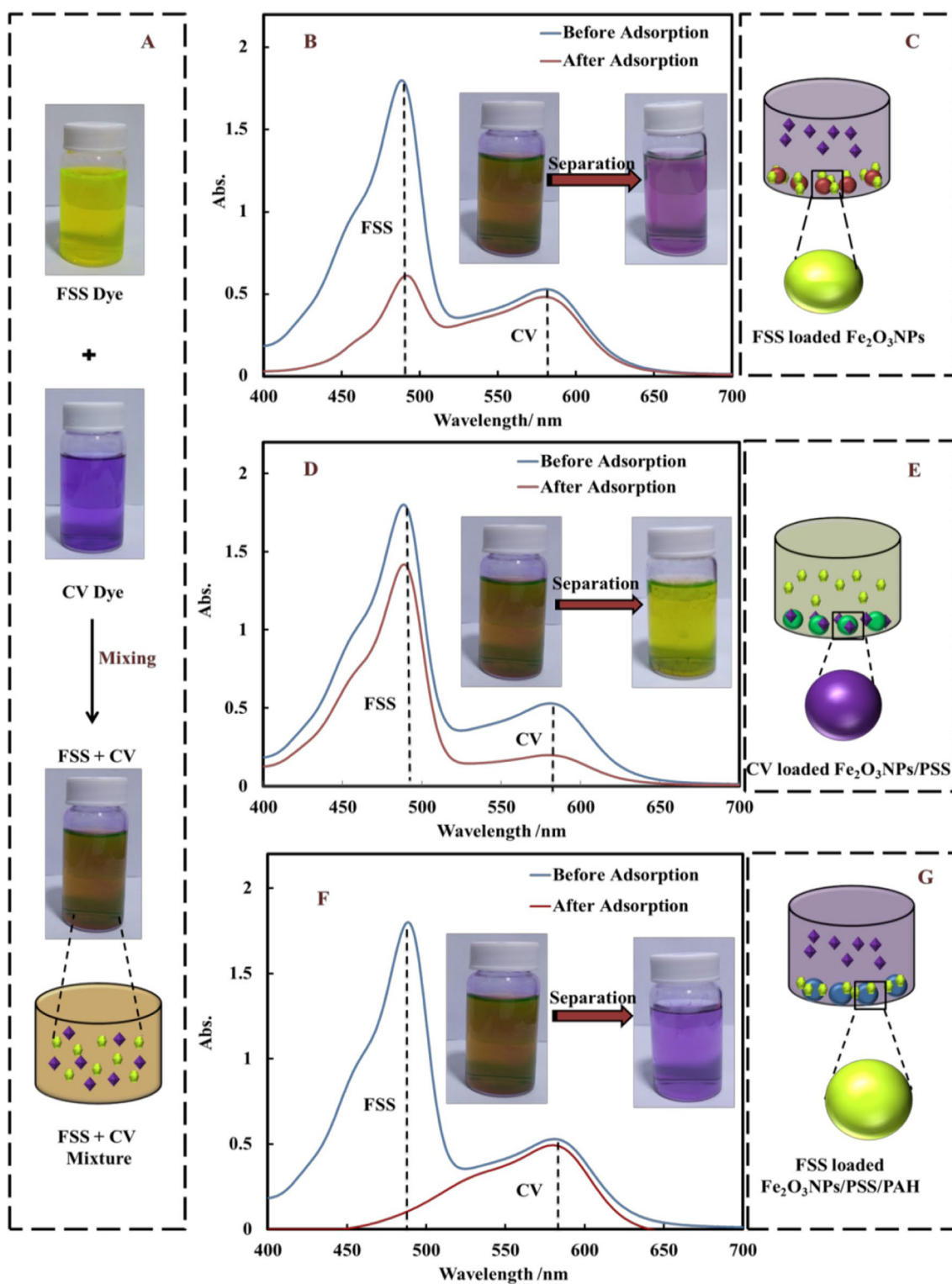
Fig. 10 Schematic diagram showing the selective removal and adsorption of Fe₂O₃NPs, Fe₂O₃NPs/PSS, Fe₂O₃NPs/PSS/PAH with FSS/CV dye. **A** Photo of FSS/CV mixture solutions. UV–Vis spectra of FSS/CV mixture solutions before and after adsorption on the **B** bare Fe₂O₃NPs; **D** Fe₂O₃NPs/PSS; **F** Fe₂O₃NPs/PSS/PAH. Photos inside Fig. **B**, **D**, **F** show the FSS/CV mixture solutions before adsorption and after adsorption. **C** FSS dye loaded Fe₂O₃NPs; **E** CV dye loaded Fe₂O₃NPs/PSS; **G** FSS dye loaded Fe₂O₃NPs/PSS/PAH
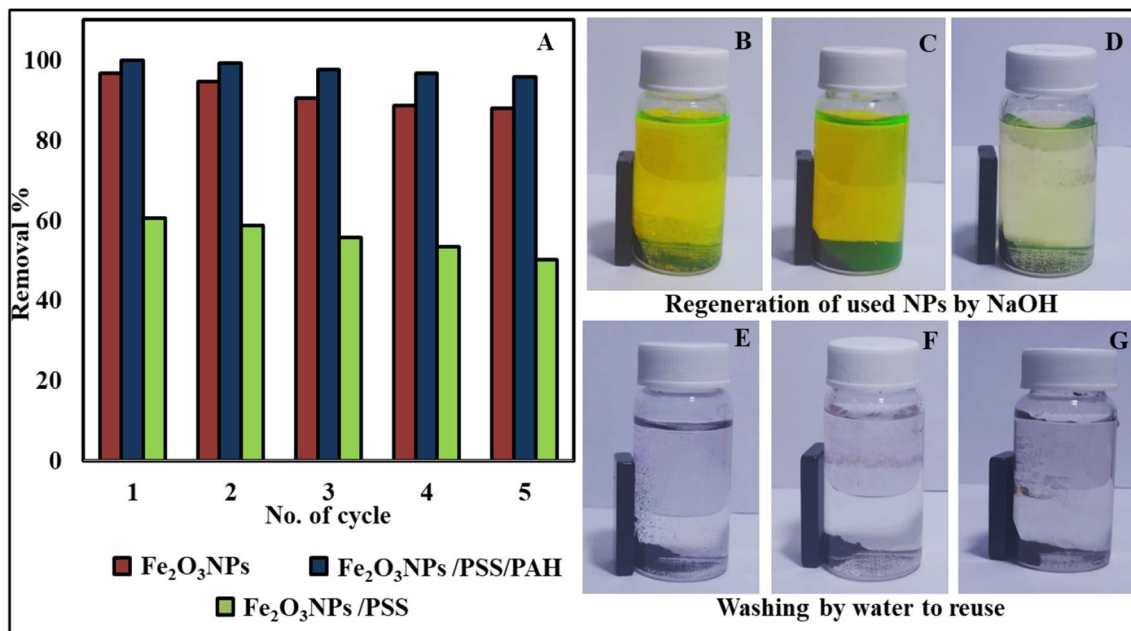
Fig. 11 **A** Reusability of bare and surface modified Fe$_2$O$_3$NPs for the removal of FSS dye. Regeneration of used **B** Fe$_2$O$_3$NPs **C** Fe$_2$O$_3$NPs/PSS/PAH and **D** Fe$_2$O$_3$NPs/PSS by NaOH. Washing of **E** Fe$_2$O$_3$NPs **F** Fe$_2$O$_3$NPs/PSS/PAH and **G** Fe$_2$O$_3$NPs/PSS by water to reuse

Materials and methods

Materials

Iron oxide nanoparticles were synthesized using iron trichloride hexahydrate (FeCl$_3$·6H$_2$O) provided by Sigma-Aldrich and ammonium hydroxide (NH$_4$OH) was bought from Fisher Scientific. Fluorescein dye was gotten from Sigma-Aldrich. Anionic polyelectrolyte (PSS, average MW of 70 kDa) and cationic polyelectrolyte (PAH, average MW of 15 kDa) were obtained from Sigma-Aldrich, UK.

Methods

Synthesis of iron oxide nanoparticles

The direct precipitation method was used for the synthesis of Fe$_2$O$_3$NPs from NH$_4$OH as a precipitating agent and FeCl$_3$·6H$_2$O as a precursor. The first step was to dissolve 4 g of FeCl$_3$·6H$_2$O in 100 cm^3 of distilled water under stirring at room temperature. Then, a 50 cm^3 aqueous solution of 2 M NH$_4$OH solution was added dropwise to the FeCl$_3$·6H$_2$O solution under stirring. The resulting black dispersion was heated for 3 h at 80 ℃ while being continuously stirred at room temperature to produce a brown powder. The resulting sediment was collected by centrifugation at 6000 rpm and washed three times with ethanol and distilled water and finally dried at 80 ℃ as shown in Fig. S1. The final product

was cooled to room temperature and calcined at (200 and 500 ℃) for 4 h [74]. All the formed nanoparticles were characterized separately, for their morphology, structural, surface properties, and chemical composition. For this purpose various techniques were used, such as Transmission Electron Microscopy (TEM), Fourier Transform Infrared (FTIR), BET, dynamic light scattering (DLS), and UV–Vis Spectrophotometer.

Preparation of polyelectrolyte-coated Fe$_2$O$_3$NPs Polyelectrolyte-coated Fe$_2$O$_3$NPs were prepared using Fe$_2$O$_3$NPs synthesized after annealing of Fe$_2$O$_3$ at 200 and 500 ℃. The first step was to disperse 2.5 g of Fe$_2$O$_3$NPs in 25 cm^3 of distilled water with sonication for 30 min at room temperature. Fe$_2$O$_3$NPs dispersion was added dropwise to an equal volume of 2.5 g in 25 cm^3 anionic polyelectrolyte PSS solution in 1 mM NaCl. The samples were homogenized for 1 h on an orbital shaker, and then the excess PSS was removed by centrifuging them for 1 h at 8000 rpm after being rinsed three times with distilled water. The zeta potential distributions and particle size of the Fe$_2$O$_3$NPs/PSS particles were measured after they had been resuspended in 25 cm^3 of distilled water. The Fe$_2$O$_3$NPs/PSS suspension was added dropwise into 2.5 g in 25 cm^3 of cationic polyelectrolyte PAH solution that was dissolved in 1 mM NaCl to create PAH-coated Fe$_2$O$_3$NPs. The formed nanoparticles was shaken for 1 h and centrifuged three times for 1 h at 8000 rpm to create

Fe$_2$O$_3$NPs/PSS/PAH [64]. The zeta potential and particle size of the surface-functionalized Fe$_2$O$_3$NPs (with PSS and PAH) were measured by dynamic light scattering.

Adsorption and photocatalytic experiments The adsorption ability of the uncoated and surface-coated Fe$_2$O$_3$NPs to adsorb dye was examined using FSS dye. A UV–Vis spectrophotometer with a 490 nm setting was used to record the experimental results. Firstly, uncoated Fe$_2$O$_3$NPs and surface-coated Fe$_2$O$_3$NPs were prepared and mixed with 100 cm^3 of FSS dye solutions. The solutions were regularly shaken for 60 min in the dark using a platform shaker as shown in Fig. S2A. We measured the absorbance at the maximum absorption wavelength both before and after adsorption. The removal percentage (R%) of FSS dye on uncoated and surface-coated Fe$_2$O$_3$NPs was calculated by batch adsorption experiment, that consisted of placing 100 cm^3 solution of 10 mg dm^{-3} of FSS dye with 0.2 g of bare and surface-coated Fe$_2$O$_3$NPs in conical flasks. The free Fe$_2$O$_3$NPs and surface-coated Fe$_2$O$_3$NPs with FSS were gently shaken in the dark at 25 ± 5 °C till they reached equilibrium. The shaker speed was set at 230 rpm. Equations (1, 3, and 4) in the Supporting Information were used to calculate the FSS removal% and the amount of FSS adsorbed per unit mass of adsorbent at equilibrium Q_e (mg g^{-1}) and at a specific time Q_t [17].

We also examined the photodegradation activity of FSS dye with bare Fe$_2$O$_3$NPs, Fe$_2$O$_3$NPs/PSS, and Fe$_2$O$_3$NPs/PSS/PAH in the presence of light. Four 15 W mercury lamps from Philips (CLEO), Poland, were used in the photocatalytic experiment, which was carried out in a photochemical reactor. The uncoated and surface-coated Fe$_2$O$_3$NPs were irradiated with FSS in conical flasks using a platform shaker as presented in Fig. S2B. In all of the photodegradation experiments, 0.2 g of uncoated and surface-coated Fe$_2$O$_3$NPs was suspended in 100 cm^3 of an aqueous solution of FSS dye. After illumination, 3 cm^3 of the reaction suspension was taken, and the bare Fe$_2$O$_3$NPs, Fe$_2$O$_3$NPs/PSS, and Fe$_2$O$_3$NPs/PSS/PAH were extracted by spinning the mixture for 15 min at 4000 rpm in a centrifuge. A second centrifugation was found to be necessary to separate out small bare and surface-coated Fe$_2$O$_3$NPs particles [17]. After the second centrifugation, the absorbance of FSS at 490 nm was recorded. The photodegradation efficiency (PDE) of FSS was also calculated according to Eq. (2) in the Supporting Information.

References

1. Normi NI, Abdulhameed AS, Jawad AH, Surip SN, Razuan R, Ibrahim ML (2023) Hydrothermal-assisted grafting of schiff base chitosan by salicylaldehyde for adsorptive removal of acidic dye: statistical modeling and adsorption mechanism. J Polym Environ 31:1925–1937

2. Sahare SP, Zodape SP (2023) Removal of Cu (II) and Cd (II) ions from aqueous solutions by methionine functionalized cobalt-magnesium ferrite chitosan beads: performance and adsorption mechanism. J Polym Environ 31:1967–1985

3. Naserzade SM, Shahrousvand M, Mohammadi-Rovshandeh J, Basati H (2023) Preparation and optimization of photocatalytic polyacrylic Acid/Guar Gum/TiO$_2$ hydrogels for absorption and removing of methylene blue under visible and UV irradiation. J Polym Environ 31:2014–2031

4. Idrees H, Halbus AF, Athab ZH, Saddam NS, Kahdum SH, Atiyah AJ (2021) Preparation and investigation of some physical properties and photocatalytic activity of a co-catalyst CoO-V$_2$O$_5$. J Phys Conf Ser. https://doi.org/10.1088/1742-6596/1999/1/012002

5. Hussein FH, Halbus AF (2012) Rapid decolorization of cobalamin. Int J PhotoenergyInternational J Photoenergy 2012:9

6. Halbus AF, Athab ZH, Hussein FH (2021) Review on preparation and characterization of activated carbon from low cost waste materials. Egypt J Chem 64:7255–7268

7. Islam T, Repon MR, Islam T, Sarwar Z, Rahman MM (2023) Impact of textile dyes on health and ecosystem: a review of structure, causes, and potential solutions. Environ Sci Pollut Res 30:9207–9242

8. Kondaveeti S, Govindarajan D, Mohanakrishna G, Thatikayala D, Abu-Reesh IM, Min B, Nambi IM, Al-Raoush RI, Aminabhavi TM (2023) Sustainable bioelectrochemical systems for bioenergy generation via waste treatment from petroleum industries. Fuel 331:125632

9. Ajmal S, Bibi I, Majid F, Ata S, Kamran K, Jilani K, Nouren S, Kamal S, Ali A, Iqbal M (2019) Effect of Fe and Bi doping on LaCoO$_3$ structural, magnetic, electric and catalytic properties. J Mater Res Technol 8:4831–4842

10. Bhatti HN, Hayat J, Iqbal M, Noreen S, Nawaz S (2018) Bio-composite application for the phosphate ions removal in aqueous medium. J Mater Res Technol 7:300–307

11. Jamil A, Bokhari TH, Javed T, Mustafa R, Sajid M, Noreen S, Zuber M, Nazir A, Iqbal M, Jilani MI (2020) Photocatalytic degradation of disperse dye Violet-26 using TiO$_2$ and ZnO nanomaterials and process variable optimization. J Mater Res Technol 9:1119–1128

12. Noreen S, Mustafa G, Ibrahim SM, Naz S, Iqbal M, Yaseen M, Javed T, Nisar J (2020) Iron oxide (Fe$_2$O$_3$) prepared via green route and adsorption efficiency evaluation for an anionic dye: kinetics, isotherms and thermodynamics studies. J Mater Res Technol 9:4206–4217

13. Kamil AM, Abdalrazak FH, Halbus AF, Hussein FH (2014) Adsorption of bismarck brown R dye onto multiwall carbon nanotubes. J Env Anal Chem 1:2

14. Halbus AF, Lafta AJ, Athab ZH, Hussein FH (2014) Adsorption of reactive yellow dye 145 from wastewater onto iraqi zahdy and khestawy date palm seeds activated carbons. Asian J Chem 16:26

15. Iqbal M, Abbas M, Nisar J, Nazir A, Qamar A (2019) Bioassays based on higher plants as excellent dosimeters for ecotoxicity monitoring: a review. Chem Int 5:1–80

16. Halbus AF, Athab ZH, Hussein FH (2013) Adsorption of disperse blue dye on Iraqi date palm seeds activated carbon. Int J Chem Sci 11:1219–1233

17. Halbus AF, Athab ZH, Abbas AS, Khaleel AK, Wahhoodee SM, Atiyah AJ (2022) Adsorption, photodegradation, and selective

removal of reactive red 2 dye onto cuprous oxide nanoparticles. Monatshefte für Chemie-Chemical Mon 153:597–607

18. Alkherraz AM, Ali AK, Elsherif KM (2020) Removal of Pb (II), Zn (II), Cu (II) and Cd (II) from aqueous solutions by adsorption onto olive branches activated carbon: equilibrium and thermodynamic studies. Chem Int 6:11–20

19. Noreen S, Bhatti HN, Iqbal M, Hussain F, Sarim FM (2020) Chitosan, starch, polyaniline and polypyrrole biocomposite with sugarcane bagasse for the efficient removal of Acid Black dye. Int J Biol Macromol 147:439–452

20. Halbus AF, Salman JM, Lafta AJ, Athab ZH, Hasan FM, Kamil AM, Hussein FH (2017) Equilibrium, isotherms and thermodynamic studies of congo red adsorption onto Ceratophyllum Demersum. Indian J Chem Technol 24:82–87

21. Ismael HI, Halbus AF, Mohammad TAH, Baqir SJ, Athab ZH, Atiyah AJ, Kadhim SH, Mohammad EJ (2022) Fabrication of carbon nanotube (CNTs)/Co3O4-Ni3O4/Al2O3 nanocomposite catalyst and its application for photocatalytic removal of Celestine blue dye. Egypt J Chem 65:99–110

22. Ahmed LM, Alkaim AF, Halbus AF, Hussein FH (2016) Photocatalytic hydrogen production from aqueous methanol solution over metallized TiO2. Int J ChemTech Res 9:90–98

23. Hassaan MA, El Nemr A, Hassaan A (2017) Health and environmental hazards of synthetic dyes. Am J Environ Sci Eng 1:64–67

24. Kamaraj M, Kidane T, Muluken KU, Aravind J (2019) Biofabrication of iron oxide nanoparticles as a potential photocatalyst for dye degradation with antimicrobial activity. Int J Environ Sci Technol 16:8305–8314

25. Hussein FH, Halbus AF, Abdalrazak FH, Athab ZH (2013) Adsorption of cobalamin onto synthesized carbon nanotubes (CNT). J Appl e Chem 2:589–604

26. Lafta AJ, Halbus AF, Athab ZH, Kamil AM, Hussein AS, Qhat AF, Hussein FH (2014) Effects of activators on adsorption ability of reactive yellow-145 dye on activated carbon from iraqi zahdi date palm seeds. Asian J Chem 16:26

27. Athab ZH, Halbus AF, Abbas AS, Salman JM, Atiyah AJ (2022) Enhanced macroporous cationic chitosan hydrogel by freezing and thawing method with superadsorption capacity for anionic dyes. J Polym Environ 30:3815–3831

28. Hussein FH, Halbus AF, Hassan HAK, Hussein WAK (2010) Photocatalytic degradation of bismarck brown G using irradiated ZnO in aqueous solutions. E-Journal Chem 7:540–544

29. Hussein FH, Halbus AF, Lafta AJ, Athab ZH (2015) Preparation and characterization of activated carbon from Iraqi Khestawy date palm. J Chem 2015:8

30. Silambarasu A, Manikandan A, Balakrishnan K (2017) Room-temperature superparamagnetism and enhanced photocatalytic activity of magnetically reusable spinel ZnFe2O4 nanocatalysts. J Supercond Nov Magn 30:2631–2640

31. Al Banna LS, Salem NM, Jaleel GA, Awwad AM (2020) Green synthesis of sulfur nanoparticles using Rosmarinus officinalis leaves extract and nematicidal activity against Meloidogyne javanica. Chem Int 6:137–143

32. Halbus AF, Horozov TS, Paunov VN (2017) Colloid particle formulations for antimicrobial applications. Adv Colloid Interface Sci 249:134–148

33. Halbus AF, Horozov TS, Paunov VN (2019) Controlling the antimicrobial action of surface modified magnesium hydroxide nanoparticles. Biomimetics 4:41

34. Karam FF, Hussein FH, Baqir SJ, Halbus AF, Dillert R, Bahnemann D (2014) Photocatalytic degradation of anthracene in closed system reactor. Int J Photoenergy 2014:6

35. Halbus AF, Horozov TS, Paunov VN (2019) Self-grafting copper oxide nanoparticles show a strong enhancement of their anti-algal and anti-yeast action. Nanoscale Adv 1:2323–2336

36. Alshehri A, Malik MA, Khan Z, Al-Thabaiti SA, Hasan N (2017) Biofabrication of Fe nanoparticles in aqueous extract of Hibiscus sabdariffa with enhanced photocatalytic activities. RSC Adv 7:25149–25159

37. Shameli K, Bin AM, Jazayeri SD, Sedaghat S, Shabanzadeh P, Jahangirian H, Mahdavi M, Abdollahi Y (2012) Synthesis and characterization of polyethylene glycol mediated silver nanoparticles by the green method. Int J Mol Sci 13:6639–6650

38. Henry P, Halbus AF, Athab ZH, Paunov VN (2021) Enhanced antimould action of surface modified copper oxide nanoparticles with phenylboronic acid surface functionality. Biomimetics 6:19

39. Halbus AF, Hussein FH (2014) Photocatalytic decolorization of cobalamin in aqueous suspensions of TiO2 and ZnO under solar irradiation. Asian J Chem 26:2014

40. Kamil AM, Hussein FH, Halbus AF, Bahnemann DW (2014) Preparation, characterization, and photocatalytic applications of MWCNTs/TiO2 composite. Int J Photoenergy 2014:8

41. Halbus AF, Horozov TS, Paunov VN (2019) Strongly enhanced antibacterial action of copper oxide nanoparticles with boronic acid surface functionality. ACS Appl Mater Interfaces 11:12232–12243

42. Izadiyan Z, Shameli K, Miyake M, Hara H, Mohamad SE, Kalantari K, Taib SH, Rasouli E (2020) Cytotoxicity assay of plant-mediated synthesized iron oxide nanoparticles using Juglans regia green husk extract. Arab J Chem 13:2011–2023

43. Weldick PJ, Wang A, Halbus AF, Paunov VN (2022) Emerging nanotechnologies for targeting antimicrobial resistance. Nanoscale 14:4018–4041

44. Laurent S, Forge D, Port M, Roch A, Robic C, Vander Elst L, Muller RN (2008) Magnetic iron oxide nanoparticles: synthesis, stabilization, vectorization, physicochemical characterizations, and biological applications. Chem Rev 108:2064–2110

45. Hu Y, Mignani S, Majoral JP, Shen M, Shi X (2018) Construction of iron oxide nanoparticle-based hybrid platforms for tumor imaging and therapy. Chem Soc Rev 47:1874–1900

46. Jeon M, Halbert MV, Stephen ZR, Zhang M (2021) Iron oxide nanoparticles as T1 contrast agents for magnetic resonance imaging: fundamentals, challenges, applications, and prospectives. Adv Mater 33:1906539

47. Zhao J, Li X, Wang X (2019) Fabrication of hybrid nanostructures based on Fe3O4 nanoclusters as theranostic agents for magnetic resonance imaging and drug delivery. Nanoscale Res Lett 14:1–12

48. Oh JK, Park JM (2011) Iron oxide-based superparamagnetic polymeric nanomaterials: design, preparation, and biomedical application. Prog Polym Sci 36:168–189

49. Verma J, Warsame C, Seenivasagam RK, Katiyar NK, Aleem E, Goel S (2023) Nanoparticle-mediated cancer cell therapy: basic science to clinical applications. Cancer Metastasis Rev 24:1–27

50. Setia A, Mehata AK, Malik AK, Viswanadh MK, Muthu MS (2023) Theranostic magnetic nanoparticles: synthesis, properties, toxicity, and emerging trends for biomedical applications. J Drug Deliv Sci Technol 21:104295

51. Lu A, Salabas EL, Schüth F (2007) Magnetic nanoparticles: synthesis, protection, functionalization, and application. Angew Chemie Int Ed 46:1222–1244

52. Pankhurst QA, Connolly J, Jones SK, Jjj D (2003) Applications of magnetic nanoparticles in biomedicine. J Phys D Appl Phys 36:R167

53. Wu W, He Q, Jiang C (2008) Magnetic iron oxide nanoparticles: synthesis and surface functionalization strategies. Nanoscale Res Lett 3:397–415

54. Cândido M, Vieira P, Campos A, Soares C, Raniero L (2023) Gold-coated superparamagnetic iron oxide nanoparticles functionalized to EGF and Ce6 complexes for breast cancer diagnoses and therapy. Pharmaceutics 15:100

55. Freis B, Ramírez MDLÁ, Furgiuele S, Journe F, Cheignon C, Charbonnière LJ, Henoumont C, Kiefer C, Mertz D, Affolter-Zbaraszczuk C, Meyer F (2023) Bioconjugation studies of an EGF-R targeting ligand on dendronized iron oxide nanoparticles to target head and neck cancer cells. Int J Pharm 635:122654

56. Schneider G, Decher G (2008) Functional core/shell nanoparticles via layer-by-layer assembly. Investigation of the experimental parameters for controlling particle aggregation and for enhancing dispersion stability. Langmuir 24:1778–1789

57. Sun B, Zhang Y, Gu KJ, Shen QD, Yang Y, Song H (2009) Layer-by-layer assembly of conjugated polyelectrolytes on magnetic nanoparticle surfaces. Langmuir 25:5969–5973

58. Johnston APR, Cortez C, Angelatos AS, Caruso F (2006) Layer-by-layer engineered capsules and their applications. Curr Opin Colloid Interface Sci 11:203–209

59. Rawtan D, Agrawal YK (2014) Emerging strategies and applications of layer-by-layer self-assembly. Nanobiomedicine 1:1–8

60. Krass H, Papastavrou G, Kurth DG (2003) Layer-by-layer self-assembly of a polyelectrolyte bearing metal ion coordination and electrostatic functionality. Chem Mater 15:196–203

61. Visakh PM (2014) Polyelectrolyte: thermodynamics and rheology: state of art, new challenges and opportunities. Springer International Publishing, Berlin, pp 1–17

62. Carneiro-da-Cunha MG, Cerqueira MA, Souza BWS, Teixeira JA, Vicente AA (2011) Influence of concentration, ionic strength and pH on zeta potential and mean hydrodynamic diameter of edible polysaccharide solutions envisaged for multinanolayered films production. Carbohydr Polym 85:522–528

63. Guzmán E, Cavallo JA, Chuliá-Jordán R, Gómez C, Strumia MC, Ortega F, Rubio RG (2011) pH-induced changes in the fabrication of multilayers of poly (acrylic acid) and chitosan: fabrication, properties, and tests as a drug storage and delivery system. Langmuir 27:6836–6845

64. Halbus AF, Horozov TS, Paunov VN (2020) Surface-modified zinc oxide nanoparticles for antialgal and antiyeast applications. ACS Appl Nano Mater 3:440–451

65. Mendoza-Dorantes T, Pal U, Vega-Acosta JR, Marquez-Beltran C (2013) Encapsulation and surface charge manipulation of organic and inorganic colloidal substrates by multilayered polyelectrolyte films. Colloids Surfaces A Physicochem Eng Asp 434:253–259

66. Márquez-Beltrán C, Castañeda L, Enciso-Aguilar M, Paredes-Quijada G, Acuña-Campa H, Maldonado-Arce A, Argillier JF (2013) Structure and mechanism formation of polyelectrolyte complex obtained from PSS/PAH system: effect of molar mixing ratio, base–acid conditions, and ionic strength. Colloid Polym Sci 291:683–690

67. Palomec-Garfias AF, Jardim KV, Sousa MH, Márquez-Beltrán C (2018) Influence of polyelectrolyte chains on surface charge and magnetization of iron oxide nanostructures. Colloids Surfaces A Physicochem Eng Asp 549:13–24

68. Liu H, Li P, Lu B, Wei Y, Sun Y (2009) Transformation of ferrihydrite in the presence or absence of trace Fe (II): the effect of preparation procedures of ferrihydrite. J Solid State Chem 182:1767–1771

69. Jing Z, Wu S (2004) Synthesis and characterization of monodisperse hematite nanoparticles modified by surfactants via hydrothermal approach. Mater Lett 58:3637–3640

70. Darezereshki E (2011) One-step synthesis of hematite (α-Fe$_2$O$_3$) nano-particles by direct thermal-decomposition of maghemite. Mater Lett 65:642–645

71. Lassoued A, Lassoued MS, Dkhil B, Ammar S, Gadri A (2018) Photocatalytic degradation of methylene blue dye by iron oxide (α-Fe$_2$O$_3$) nanoparticles under visible irradiation. J Mater Sci Mater Electron 29:8142–8152

72. Rápó E, Tonk S (2021) Factors affecting synthetic dye adsorption; desorption studies: a review of results from the last five years (2017–2021). Molecules 26:5419

73. Tamirat AG, Rick J, Dubale AA, Su WN, Hwang BJ (2016) Using hematite for photoelectrochemical water splitting: a review of current progress and challenges. Nanoscale Horizons 1:243–267

74. Farahmandjou M, Soflaee F (2015) Synthesis and characterization of α-Fe$_2$O$_3$ nanoparticles by simple co-precipitation method. Phys Chem Res 3:191–196